

# Acoustic impedance and hydrodynamic instability of the flow through a circular aperture in a thick plate

R. Longobardi<sup>1,2</sup>, D. Fabre<sup>1†</sup>, V. Citro<sup>2</sup>, P. Bonnefis<sup>1</sup> and P. Luchini<sup>2</sup>

<sup>1</sup>Institut de Mécanique des Fluides de Toulouse, IMFT, Université de Toulouse, CNRS; Allée Camille Soula, 31400 Toulouse, France

<sup>2</sup>DIIN, Università degli Studi di Salerno, Via Giovanni Paolo II, 84084 Fisciano (SA), Italy

(Received xx; revised xx; accepted xx)

We study the unsteady flow of a viscous fluid passing through a circular aperture in a plate characterized by a non-zero thickness. We investigate this problem by solving the incompressible Linearized Navier-Stokes Equations (LNSE) around a laminar base flow, in both the forced regime (allowing to characterize the coupling of the flow with acoustic resonators) and the autonomous regime (allowing to identify the possibility of purely hydrodynamical instabilities). In the forced regime, we calculate the impedances and discuss the stability properties in terms of a Nyquist diagram. We show that such diagrams allow to predict two kinds of instabilities: (*i*) a conditional instability linked to the overreflexion of an acoustic wave but requiring the existence of an conveniently tuned external acoustic resonator, and (*ii*) a purely hydrodynamic instability existing even in a strictly incompressible framework. A parametric study is conducted to predict the range of existence of both instabilities in terms of the Reynolds number and the aspect ratio of the aperture. Analysing the structure of the linearly forced flow allows to show that the instability mechanism is closely linked to the existence of a recirculation region within the thickness of the plate. We then investigate the autonomous regime using a standard normal-mode analysis. The analysis confirms the existence of the purely hydrodynamical instability in accordance with the impedance-based criterion. The spatial structure of the unstable eigenmodes are found to be similar to the structure of the corresponding unsteady flows computed using the forced problem. Analysis of the adjoint eigenmodes and of the adjoint-based structural sensitivity confirms that the origin of the instability lies in the recirculation region existing within the thickness of the plate.

**Key words:** Instabilities, Jets, Acoustic impedance

## 1. Introduction

The unsteady flow through an aperture separating two fluid domains, either closed (ducts, chambers, resonators) or open, is encountered in a large number of applications. This situation is also of fundamental importance in the design of musical instruments. A fundamental milestone in the study of such problems is the classical Rayleigh (1945) solution of the inviscid, potential flow through a circular hole, in the absence of mean flow. This solution shows that the situation is globally equivalent to the simple assumption

† Email address for correspondence: david.fabre@imft.fr

of a rigid plug of fluid with an "effective length"  $l_{eff}$  oscillating across the aperture. This Rayleigh solution is often invoked in simple models of acoustic devices and is, for instance, a key ingredient in the modelling of the so-called Helmholtz resonator.

In the case where the aperture is traversed by a mean flow, the fluid no longer behaves as an ideal, rigid plug but generally acts as an energy dissipator. This property is used in many industrial applications where one wants to suppress acoustical waves (see for instance the bibliography cited in Fabre *et al.* (2018a)). This energy dissipation is generally associated to a transfer of energy to the flow through the excitation of vortical structures along the shear layer bounding the jet. The situation was investigated theoretically by Howe (1979), who introduced a complex quantity called *conductivity*  $K_R$  which generalizes Rayleigh's "effective length". The knowledge of  $K_R(\omega)$  as function of the forcing frequency  $\omega$ , or of the closely related quantity  $Z(\omega) = -i\omega/K_R(\omega)$  called the *impedance*, allows to fully characterize the possible interaction of the flow with acoustic waves. In particular, the real part of the impedance (which is positive for a zero-thickness hole), is directly linked to the energy flux transferred from the waves to the flow. Howe subsequently derived a potential model predicting the conductivity (and impedance) in the case of a hole of zero thickness. Despite its mathematical rigour, Howe's model starts from very simplified hypotheses regarding the shape and the location of the vortex sheet and its convective velocity. Recently, Fabre *et al.* (2018a) reviewed Howe's problem using Linearized Navier–Stokes equations in order to take into account the effect of the viscosity and the exact shape of the vortex sheet. They showed that for  $Re \gtrsim 1500$ , results are quite independent from the Reynolds number but significantly deviates from the Howe's ones, above all for intermediate frequencies. Nevertheless, in both Howe's model and Fabre *et al.* (2018a)'s improved solution, the behaviour of the hole remains dissipative (associated to a positive real part of the impedance), in accordance with experimental and numerical investigations.

The case where the thickness of the plate in which the hole is drilled is not small compared to its diameter leads to a completely different situation, as the jet flow can now act as a *sound generator* instead of a sound attenuator. The first observation of this property seems to have been made by Bouasse (1929), who reported that jets through thick plates could produce a well-reproducible whistling, with a frequency roughly proportional to the hole thickness. This observation remained unnoticed (as many other findings of the surprisingly rich experimental work of Bouasse), but was rediscovered in the 21th century by Jing & Sun (2000) and Su *et al.* (2015) who, in an effort to improve the design of perforated plates used as sound dampers, reported that in some circumstances, these devices could lose their ability to damp acoustic waves and lead to self-sustained whistlings. Numerical simulations by Kierkegaard *et al.* (2012) showed that in the range of parameters where such whistlings occur, the mean flow through the hole is characterized by a recirculation bubble, either trapped within the thickness of the plate, or fully detached. However, the precise role of this recirculation bubble in the sound-production phenomenon remains to be clarified.

The ability of the jet flow to provide acoustical energy is associated to a positive real part of the impedance, so computation or measurement of this quantity offers a convenient way to characterise these phenomena. A number of analytical and semi–empirical models (Jing & Sun (2000), Bellucci *et al.* (2004)) have been proposed to predict the impedance of such finite-length holes. Confrontation with experiments Su *et al.* (2015) and numerical simulations Eldredge *et al.* (2007) have revealed the lack of robustness of such models which all contain *ad-hoc* parameters. Yang & Morgans (2016) developed a more elaborate semi–analytical model based on the actual shape of the vortex sheet, and furthermore including the effect of compressibility within the thickness of the hole. However, their

approach remains potential and cannot account for the effect of viscosity within the thickness of the shear layer, nor for the dependence of the impedance with respect to the Reynolds number.

Linearised Navier-Stokes Equations (LNSE), offers a more satisfying framework to access the impedance of such holes, with a full incorporation of viscous effects. As already pointed out, this approach has been carried out in Fabre *et al.* (2018a) for a zero-thickness hole, leading to notable improvements of Howe's classical inviscid model. This approach has also been applied to the flow through a finite-thickness hole by Kierkegaard *et al.* (2012) in a range of parameters characterized by self-sustained whistlings. These authors also showed that computation of the impedance for a forced problem (with real  $\omega$ ) can be used, thanks to Nyquist diagrams, to predict an instability criterion for eigenmodes (with complex  $\omega$ ) of the unforced, self-sustained problem. A similar approach will be carried out in the present paper. However, our work differs from that of Kierkegaard *et al.* (2012) by a number of points. First, Kierkegaard *et al.* (2012) considered a constriction within a long pipe, while we consider a small aperture connecting an upstream and a downstream domain considered of large dimension. Secondly, Kierkegaard *et al.* (2012) considered a case where the Mach number based on the maximum velocity is not small and used compressible LNSE. On the other hand, our study starts from the incompressible equations under an acoustical compactness hypothesis. Third, Kierkegaard *et al.* (2012) considered a High-Reynolds turbulent situation and built their linearized approach around a mean flow obtained by RANS simulations. On our side, we consider a lower range of Reynolds number and build our approach around a laminar base flow consistent with the LNSE framework. Finally Kierkegaard *et al.* (2012) explicitly considered the coupling with an acoustic resonator by introducing a wave reflection condition at the inlet of the pipe, and hence their Nyquist-based stability criterion is only relevant to this situation. In our case, we wish to characterize the potential of the jet to lead to self-sustained oscillations regardless of the nature of the acoustic environment, and even in the case where there are no acoustic resonators at all. The situation we investigate is thus more simple and "academic", but by ruling out the geometry of the upstream and downstream domains and the Mach number parameter, we are able to conduct a full parametric study of the problem, an objective which was not achievable considering the choices of Kierkegaard *et al.* (2012).

The remainder of the paper is organized as follows :

- In section 2, after defining the geometry and the parameters of the study, we define the concept of impedance, and explain how, thanks to the use of Nyquist diagrams, this quantity can be used to predict the stability properties of the jet flow. We show that two kinds of instabilities are possible in this context : (i) a *conditional instability* corresponding to an overreflexion of acoustic waves in some range of frequencies, leading to an effective instability only if the jet is coupled to a conveniently tuned acoustic resonator, and (ii) a *purely hydrodynamical instability* which manifests regardless of the existence of an acoustic resonator, and exists even in the case of a strictly incompressible flow.
- In section 3, we recall the Linearized Navier Stokes Equations, and the numerical resolution method, as already presented in Fabre *et al.* (2018a). We show how this formalism can be used to solve both a harmonically forced problem for real frequencies  $\omega$  allowing to compute the impedances, and a homogeneous eigenvalue problem allowing to compute the complex frequencies  $\omega_r + i\omega_i$  allowing to characterize the purely hydrodynamical instabilities.
- In section 4, we detail the structure of the base flow corresponding to the steady jet as function of the Reynolds number  $Re$  and aspect ratio  $\beta$  of the hole. We detail

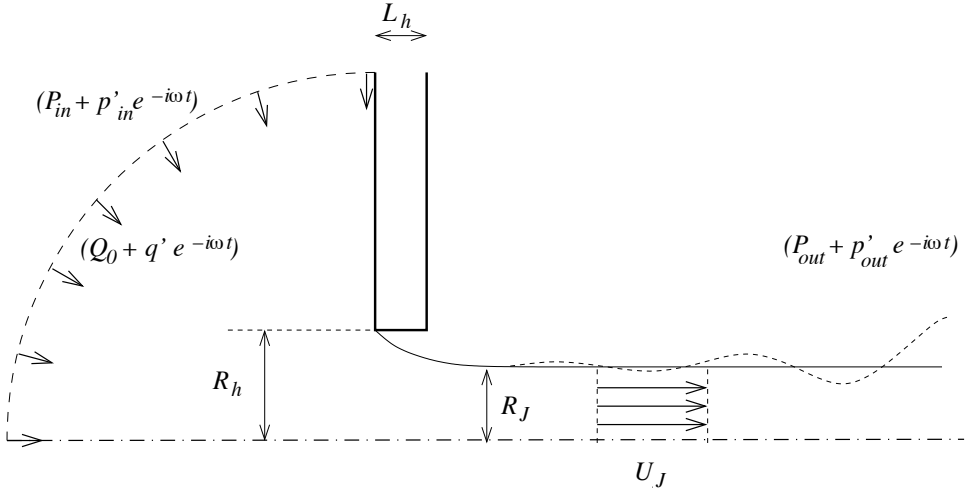


FIGURE 1. Sketch of the flow configuration (not in scale) representing the oscillating flow through a circular hole in a thick plate and definition of the geometrical parameters. We report also the decomposition of the flow quantities in the upstream and downstream boundaries.

in particular the *Venna contracta* coefficient characterizing the relationship between the mean pressure drop and mean flux through the hole, and the range of existence and spatial structure of the recirculation region which forms within the thickness of the hole.

- In section 5, we present results of the LNSE approach in the harmonically forced regime. We present the computed impedances for selected values of  $Re$  and  $\beta$ . We document the structure of the linearly forced flows, in particular within the recirculation region. We eventually provide a parametric map allowing to predict the ranges of existence of both conditional and hydrodynamical instabilities in the  $Re - \beta$  parameter plane.

- In section 6, we present results of the LNSE approach in the homogeneous regime. We confirm the existence of the purely hydrodynamical instability, in accordance with the impedance-based predictions. We further detail the structure of the eigenmodes, the adjoint eigenmodes and the adjoint-based structural sensitivity, allowing to highlight once again the role of the recirculation region on the instability mechanism.

- Finally, section 7 summarizes the findings and discusses a few perspectives opened by our work.

## 2. Problem definition

### 2.1. Geometry, parameters, and modelling hypotheses

The situation investigated in the present paper is sketched in figure 1. We consider a fluid of viscosity  $\nu$  and density  $\rho$  discharging through a circular aperture of radius  $R_h$  in a planar thick plate with thickness  $L_h$ . The domains located upstream and downstream of the hole are supposed of large dimensions compared to the dimensions of the hole, so that the geometry is characterized by a single dimensionless parameter, the aspect ratio  $\beta$  defined as

$$\beta = \frac{L_h}{2R_h}. \quad (2.1)$$

The zero-thickness limit case ( $\beta = 0$ ) is investigated in detail in Fabre *et al.* (2018a); in the present paper we consider holes with finite thickness in the range  $\beta \in [0.1 - 2]$ .

The pressure difference between the inlet and the outlet domain, namely  $\Delta P = [P_{in} - P_{out}]$ , generates a net flow  $Q = U_M A_h$  through the hole, where  $A_h = \pi R_h^2$  is the area of the hole and  $U_M$  is the mean velocity. This mean flow is characterized by a Reynolds number defined as :

$$Re = \frac{2R_h U_M}{\nu} \equiv \frac{2Q}{\pi R_h \nu}. \quad (2.2)$$

Following Fabre *et al.* (2018a), we will suppose that the mean Mach number is small, and that the dimensions of the hole are small compared to the acoustical wavelengths (acoustical compactness hypothesis). These hypotheses allow to assume that the flow is locally incompressible in the region of the hole. An example of matching with an outer acoustic field is presented in appendix A.

## 2.2. Characterization of the unsteady regime and Impedance definition

To characterize the behaviour of the jet in the unsteady regime, we assume that far away from the hole the pressure levels in the upstream and downstream regions tend to uniform values denoted as  $p_{in}(t)$  and  $p_{out}(t)$ . We will further assume that both the pressure drop  $\Delta p(t)$  and the flow rate  $q(t)$  are perturbed by a small-amplitude deviations from the mean state characterized by a frequency  $\omega$  (possibly complex):

$$\begin{pmatrix} \Delta p(t) \\ q(t) \end{pmatrix} = \begin{pmatrix} [P_{in} - P_{out}] \\ Q \end{pmatrix} + \varepsilon \begin{pmatrix} [p'_{in} - p'_{out}] \\ q' \end{pmatrix} e^{-i\omega t} + c.c., \quad (2.3)$$

$$Z_h(\omega) = \frac{[p'_{in} - p'_{out}]}{q'} \quad (2.4)$$

Note that with the present definition the impedance has physical dimensions  $M \cdot T^{-1} L^{-4}$ . We will also introduce a nondimensional impedance defined as

$$Z = \frac{R_h^2}{\rho U_M} Z_h \equiv Z_R + i Z_I, \quad (2.5)$$

where the real part of the impedance  $Z_R$  is the dimensionless resistance while its imaginary part  $Z_I$  is the reactance. In presentation of the results, the frequency will be represented in a nondimensional way by introducing the Strouhal number  $\Omega$  as follows:

$$\Omega = \frac{\omega R_h}{U_M}. \quad (2.6)$$

As already stated in the introduction, the sign of the real part of the impedance  $Z_R$  (or *resistance*) is directly proportional to the energy flux  $\langle \Pi \rangle$  transferred to the flow through  $\langle \Pi \rangle = 2\rho U_M / (R_h^2) Z_R |q'|^2$ . The demonstration of this property can be found in Howe (1979), and is also reproduced in Fabre *et al.* (2018a).

## 2.3. Impedance-based instability criteria

We now explain the links between impedance and instabilities, and show how simple instability criteria can be formulated using Nyquist diagrams (namely representations of  $Z_r$  versus  $Z_i$ ).

- First, as already discussed, the sign of the real part of the impedance  $Z_R(\omega)$  (or *resistance*) as function of the *real* frequency  $\omega$  is a direct indicator of a possible instability. However, one should insist that the condition  $Z_R < 0$  is a necessary but not sufficient

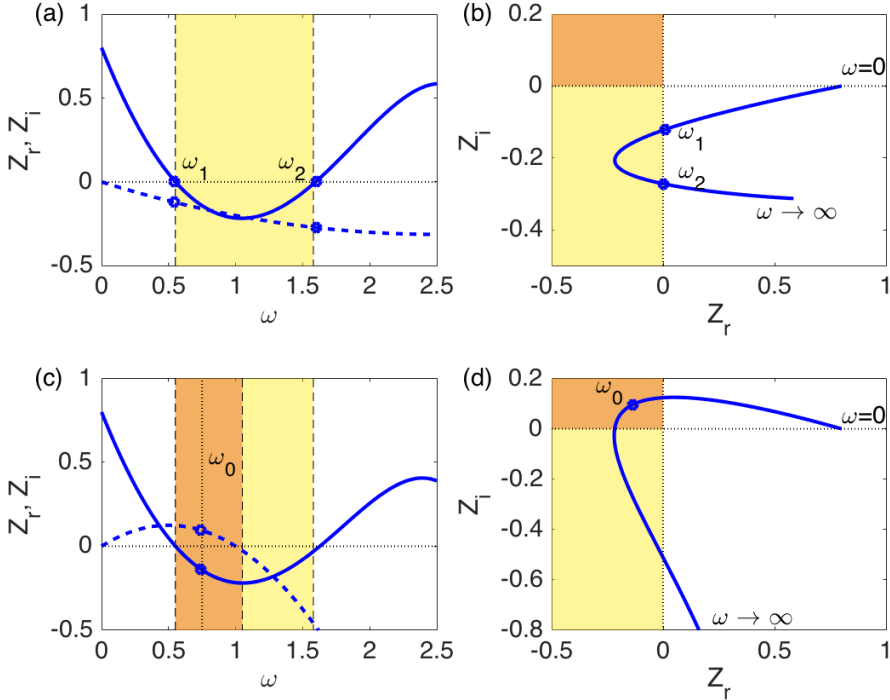


FIGURE 2. (a) and (b) example of situation leading to conditional instability. (c) and (d) example of situation leading to hydrodynamical instability. The regions of conditional and hydrodynamic instabilities are represented by yellow and orange areas, respectively.

condition for instability. In the context of electrical circuits (Conciauro & Puglisi (1981)), a system with negative resistance is said to be *active* in the sense that it effectively leads to an instability if connected to a reactive circuit allowing oscillations in the right range of frequencies. In the present context, this situation is referred as *conditional instability* and requires the presence of a correctly tuned acoustic oscillator (a cavity and/or a pipe) connected upstream (or downstream) of the aperture.

The demonstration that  $Z_R < 0$  is a necessary condition for *conditional instability* can be explicated in two ways. First, as already stated,  $Z_R$  is directly linked to the energy flux transferred from acoustic waves to the jet. Thus, if  $Z_R > 0$  the jet behaves as an energy sink, while if  $Z_R < 0$  it acts as an energy source. Secondly, one can also establishes this link by studying the reflection of acoustic waves onto the hole. This argument is carried out in appendix A, where we conduct an asymptotic matching between the locally incompressible solution in the vicinity of the hole and an outer solution of the acoustic problem. The conclusion of this analysis is that in the limit of small Mach number, an incident acoustic wave coming from the upstream domain is overreflected if and only if  $Z_R < 0$ .

A situation leading to *conditional instability* is illustrated in figure 2a – b. Plot (a) shows the real and imaginary parts of the impedance in a situation where  $Z_R$  is negative in an interval  $[\omega_1, \omega_2]$ , and  $Z_i$  does not change sign. When represented in a Nyquist diagram, the criterion can be formulated as follows: *the system is conditionally unstable if the Nyquist curves enter the half-plane  $Z_R < 0$* .

- Secondly, when considered as an analytical function of the *complex* frequency  $\omega = \omega_r + i\omega_i$ , the impedance can be used to formulate a second instability criterion, namely: the system is unstable, regardless of the properties of its environment if there exists a complex zero of the impedance function such that  $\omega_i > 0$ . Indeed, for complex values of  $\omega$  the modal dependence reads  $e^{-i\omega t} = e^{-i\omega_r t}e^{\omega_i t}$ , thus solutions with the form 2.3 are exponentially growing if  $\omega_i > 0$ . In the context of electrical circuits, this situation is referred to as *absolute* instability in opposition to the conditional instability discussed above. Since the term "absolute" has a different meaning in the hydrodynamic stability community (as opposed to convective instabilities, see e.g. Huerre & Monkewitz (1990)), we prefer to adopt the term *purely hydrodynamical instabilities* to describe this case, emphasizing the fact that they can occur in a strictly incompressible framework.

Physically, the condition  $Z_h(\omega) = 0$  implies that there exist modal solutions of the linearized problem in which pressure jump  $[p'_{in} - p'_{out}]$  is exactly zero. In other terms, the total pressure jump across the hole is imposed as a constant (i.e.  $[p_{in}(t) - p_{out}(t)] = [P_{in} - P_{out}]$ ) but the flow rate  $q(t)$  is allowed to vary. This kind of boundary condition is a bit uncommon for incompressible flow problems. However, one must keep in mind that the incompressible solution is only valid locally in the vicinity of the hole. In appendix A, we conduct an asymptotic matching with an outer acoustic solution and show that in the limit of small Mach number, the condition  $Z_h(\omega) = 0$  with complex  $\omega$  and  $\omega_i > 0$  corresponds to a spontaneous self-oscillation of the flow across the hole associated to the radiation of acoustical waves in both the upstream and downstream domains.

In practise, the number of complex zeros of the analytically continued impedance  $Z_h(\omega)$  and their location in the complex plane can be deduced from the representation of  $Z_h(\omega)$  for real values  $\omega$  using classical Nyquist criterion, which states that *there exists an unstable zero of the impedance if and only if the Nyquist curve encircles the origin in the anticlockwise direction*. A weaker but practically equivalent version of this criterion can be formulated as follows: *the system is unstable in a purely hydrodynamical way if the Nyquist curve enters the quarter-plane defined by  $Z_R < 0$  ;  $Z_I > 0$* . A situation leading to *purely hydrodynamical instability* is illustrated in figure 2c – d.

In addition to providing an instability criterion, the knowledge of the impedance for real  $\omega$  can also be used to predict an approximation of the complex zeros in the case where  $\omega_i$  is small. for this sake, let us suppose that the Nyquist curve passes close to the origin, and let us note  $\omega_0$  the value for which the norm of the complex impedance  $|Z(\omega)|$  is smallest. The location of this point is illustrated in figures 2c – d. Searching for the complex zero as  $\omega = \omega_0 + \delta\omega$  and working with a Taylor series around  $\omega_0$  leads to  $Z(\omega_0) + (\partial Z/\partial\omega)_{\omega_0}\delta\omega = 0$ , hence providing an estimation as follows :

$$\omega \approx \omega_0 - \frac{Z(\omega_0)\overline{(\partial Z/\partial\omega)_{\omega_0}}}{|(\partial Z/\partial\omega)_{\omega_0}|^2} \quad (2.7)$$

It can be shown that  $\Re(Z(\omega_0)\overline{(\partial Z/\partial\omega)_{\omega_0}}) = 0$  (a simple geometrical interpretation being that the line joining the point  $Z(\omega_0)$  to the origin and the line tangent to the Nyquist curve at  $\omega_0$  are orthogonal to each other). Hence, the correction appearing in 2.7 directly provides an estimation of the amplification rate  $\omega_i$ .

### 3. Linearized Navier Stokes Equations and numerical methods

In the previous section, the linearly perturbed flow across a hole was considered from a general point of view, focussing on the impedance and its link with possible instabilities. In the present section, we introduce the LNSE framework, and show how this framework

can be used both to compute the impedance through resolution of a *forced problem* and to directly address the instability problem through resolution of an *autonomous problem*.

### 3.1. Starting equations

The fluid motion is governed by the Navier-Stokes equations:

$$\frac{\partial}{\partial t} \begin{bmatrix} \mathbf{u} \\ 0 \end{bmatrix} = \mathcal{NS} \begin{bmatrix} \mathbf{u} \\ p \end{bmatrix} = \begin{bmatrix} -\mathbf{u} \cdot \nabla \mathbf{u} - \nabla p + Re^{-1} \nabla^2 \mathbf{u} \\ \nabla \cdot \mathbf{u} \end{bmatrix} \quad (3.1)$$

where  $p$  is the reduced pressure field. Since we are in axial-symmetric flow configuration, we decompose the velocity vector  $\mathbf{u}$  in an axial component  $u_x$  and in a radial component  $u_r$ .

The Linearized Navier-Stokes framework consists of expanding the flow as a steady base-flow plus a small-amplitude modal perturbation as follows:

$$\begin{bmatrix} \mathbf{u} \\ p \end{bmatrix} = \begin{bmatrix} \mathbf{u}_0 \\ p_0 \end{bmatrix} + \epsilon \begin{bmatrix} \mathbf{u}' \\ p' \end{bmatrix} e^{-i\omega t}. \quad (3.2)$$

### 3.2. Base-flow equations

The base flow is the solution of the steady version of the Navier-Stokes equations:

$$\mathcal{NS}[\mathbf{u}_0; p_0] = 0$$

with the following set of boundary conditions:

$$\begin{aligned} P(x, r) &\rightarrow P_{in} \quad \text{as } x^2 + r^2 \rightarrow \infty \quad \text{and } x < 0 \\ P(x, r) &\rightarrow P_{out} \quad \text{as } x^2 + r^2 \rightarrow \infty \quad \text{and } x > 0 \\ \int_{\mathcal{S}} \mathbf{u}_0 \cdot \mathbf{n} dS &= Q. \end{aligned} \quad (3.3)$$

where  $\mathcal{S}$  is any surface traversed by the flow. It is convenient to choose  $\mathcal{S}$  as the inlet of the domain so that the latter equation can be imposed as a Dirichlet boundary condition.

### 3.3. Linear equations

The linear perturbation obeys the following equations :

$$-i\omega \mathcal{B}[\mathbf{u}'; p'] = \mathcal{L}\mathcal{NS}_0[\mathbf{u}'; p'], \quad (3.4)$$

where  $\mathcal{L}\mathcal{NS}_0$  is the linearized Navier-Stokes operator around the base flow and  $\mathcal{B}$  is a weight operator defined as follows:

$$\mathcal{L}\mathcal{NS}_0 \begin{bmatrix} \mathbf{u}' \\ p' \end{bmatrix} = \begin{bmatrix} -(\mathbf{u}_0 \cdot \nabla \mathbf{u}' + \mathbf{u}' \cdot \nabla \mathbf{u}_0) - \nabla p' + Re^{-1} \nabla^2 \mathbf{u}' \\ \nabla \cdot \mathbf{u}' \end{bmatrix}; \quad \mathcal{B} = \begin{bmatrix} 1 & 0 \\ 0 & 0 \end{bmatrix} \quad (3.5)$$

This set of equations is complemented by the following boundary conditions :

$$p'(x, r) \rightarrow p'_{in} \quad \text{for } \sqrt{x^2 + r^2} \rightarrow \infty \text{ and } x < 0, \quad (3.6)$$

$$p'(x, r) \rightarrow p'_{out} \quad \text{for } \sqrt{x^2 + r^2} \rightarrow \infty \text{ and } x > 0, \quad (3.7)$$

$$\int_{\mathcal{S}} \mathbf{u}' \cdot \mathbf{n} dS = q'. \quad (3.8)$$

This set of equations for the perturbations is relevant to both the forced problem and the autonomous problem. The difference is in the handling of the boundary conditions:

- For the *forced problem*, a non-zero  $q'$  is imposed (fixed arbitrarily to  $q' = 1$ ). Eq. (3.8) thus constitutes a non-homogeneous boundary condition at the inlet plane. On the other

hand, since only  $p'_{in} - p'_{out}$  is relevant, one can set  $p'_{out} = 0$  without loss of generality. Eq. (3.7) thus leads to a homogeneous boundary condition at the outlet plane. The problem can be symbolically written as

$$[\mathcal{LNS}_0 - i\omega \mathcal{B}] [\mathbf{u}'; p'] = \mathcal{F},$$

where the definition of  $\mathcal{LNS}_0$  implicitly contains the homogeneous boundary condition at the outlet, and  $\mathcal{F}$  represents symbolically the non-homogeneous boundary condition at the inlet. This problem is nonsingular and readily solved. The pressure jump  $p'_{in}$  allowing to define the impedance is subsequently deduced from Eq. (3.6).

- For the *homogeneous problem*, as discussed in sec. 2, the relevant boundary conditions are  $p'_{in} = p'_{out}$  and we can take  $p'_{in} = p'_{out} = 0$  without loss of generality. Thus, Eqs. (3.6) and (3.7) both lead to homogeneous boundary conditions. Using the eigenmode notation  $[\mathbf{u}', p'] = [\hat{\mathbf{u}}, \hat{p}]$  for the perturbation, the problem can be symbolically written in the form

$$[\mathcal{LNS}_0^* - i\omega \mathcal{B}] [\hat{\mathbf{u}}; \hat{p}] = 0$$

where the operator  $\mathcal{LNS}_0^*$  implicitly contains the homogeneous conditions at both upstream and downstream boundaries.

This problem is a generalized eigenvalue one, and thus admits solutions for a discrete set of complex eigenvalues  $\omega = \omega_r + \omega_i$ . The flow rate  $\hat{q}$  associated to the eigenmodes through 3.8 is generally nonzero, but the eigenmodes can be arbitrarily rescaled such that  $\hat{q} = 1$ .

Aside from the determinations of the (direct) eigenmodes  $[\hat{\mathbf{u}}, \hat{p}]$ , it is also useful to study the structure of the adjoint eigenmodes  $[\hat{\mathbf{u}}^\dagger, \hat{p}^\dagger]$ , namely the eigenmodes of the adjoint operator  $\mathcal{LNS}_0^{*\dagger}$ . The importance of adjoint eigenmodes in fluid mechanics has been reviewed by Luchini & Bottaro (2014). Here, since this concept has been largely discussed in a lot of previous papers like Citro *et al.* (2016) and Citro *et al.* (2015), we prefer to avoid to derive the adjoint problem. We refer to Luchini & Bottaro (2014) for a detailed discussion of the topic.

The structural sensitivity of a hydrodynamic oscillator is also used in the present manuscript to identify the flow region where the mechanism of instability acts. The so-called wavemaker can be spatially localized by inspecting the spatial map obtained from the sensitivity tensor:

$$\mathbf{S}(x, r) = \frac{\hat{\mathbf{u}}^\dagger(x, r) \otimes \hat{\mathbf{u}}(x, r)}{\int_D \hat{\mathbf{u}}^\dagger(x, r) \hat{\mathbf{u}}(x, r) dD} \quad (3.9)$$

where  $D$  is the computational domain. This region is responsible for the instability mechanism, i.e. one can think that the direct mode is emanated from the wavemaker region.

### 3.4. Numerical method

The results presented here are obtained with the same numerical code adopted in Fabre *et al.* (2018a). In particular, we used the open source code FreeFem++ that implements the finite-element method to solve the several problems described in the present paper. The main originalities of the present implementation are the use of complex mapping in the axial direction to overcome problems associated to the large convective amplification of structures in the downstream direction (see Fabre *et al.* (2018a)), and the systematic use of mesh adaptation to substantially reduce the required number of dof (following a methodology described in Fabre *et al.* (2018b); Fabre *et al.* (2018a)). An example of unstructured grid obtained in this way is displayed in figure 3. Note that

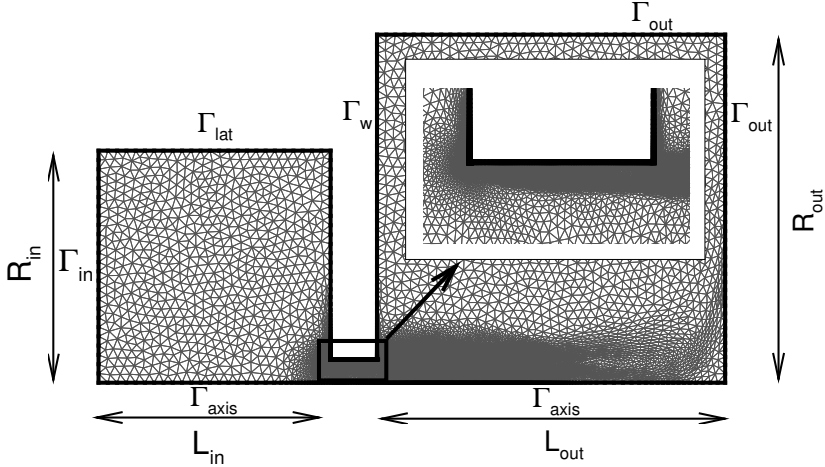


FIGURE 3. Structure of the mesh  $\mathbb{M}_1$  obtained using complex mapping and mesh adaptation for  $\beta = 1$ , and nomenclature of the boundaries (see appendix B for details on mesh generation and validation). A zoom of the mesh is reported in the range  $X \in [-2.5; 0.5]R_h$  and  $R \in [0.1; 1.8]R_h$ .

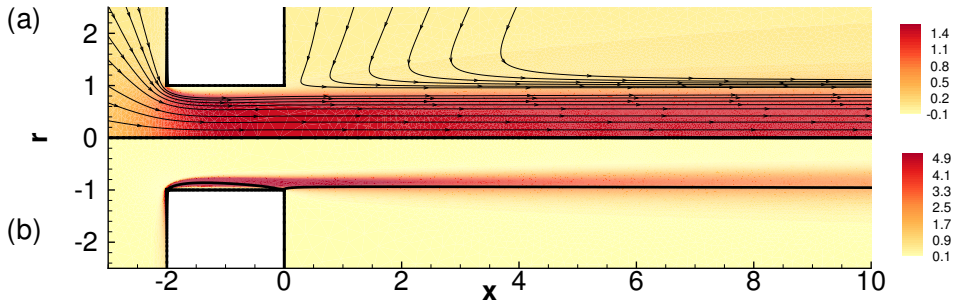


FIGURE 4. Contour plot of (a) axial velocity of the base flow and (b) vorticity field computed at  $Re = 1500$  and  $\beta = 1$ .

the downstream dimension  $L_{out}$  in numerical coordinates seems rather short; however, as the coordinate mapping used in this case involves a stretching the actual dimension in physical coordinates is much larger (see details in appendix B).

All the codes and the scripts used in the present manuscript are available online on the github page dedicated to the StabFem project ([github.com/erbafdavid/StabFem](https://github.com/erbafdavid/StabFem)). As a consequence, most of the result presented herein can be easily obtained by running the inherent script in the StabFem project. On a standard laptop, all the computations discussed below can be obtained in only a few hours. The validation of the solver and of the proposed numerical approach is presented in the review dedicated to StabFem (Fabre *et al.* 2018*b*). The complex mapping adopted in the downstream domain is discussed in detail by Fabre *et al.* (2018*a*). A brief survey about this topic is also reported in Appendix B.

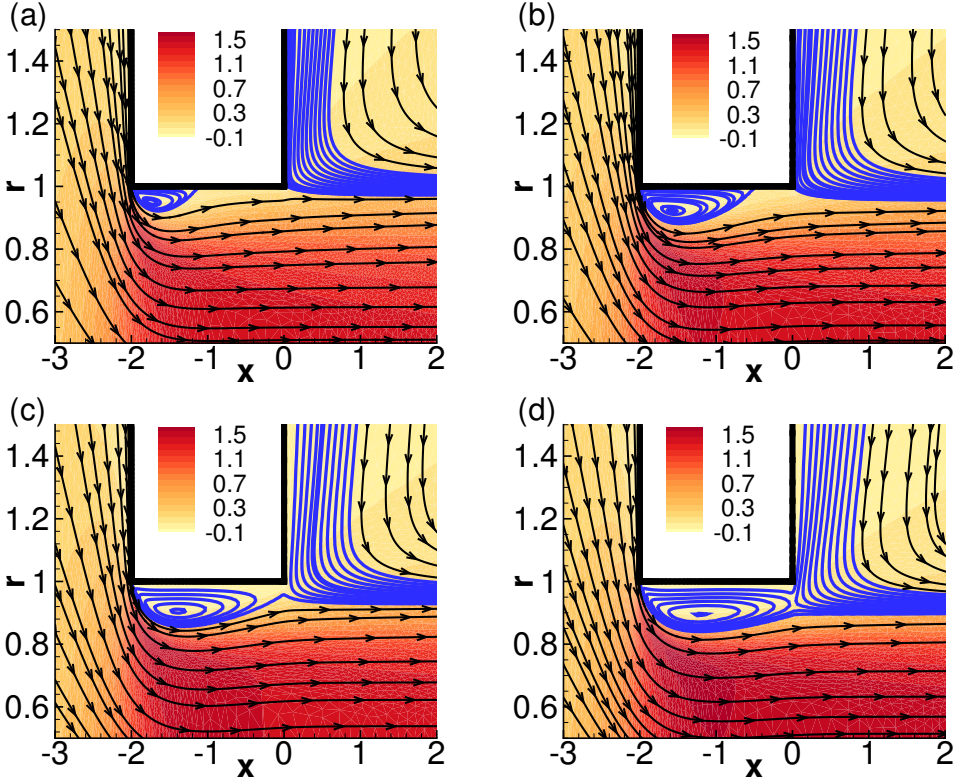


FIGURE 5. Contour plot of the axial component of the base flow at: (a)  $Re = 800$ , (b)  $Re = 1200$ , (c)  $Re = 1600$ , (d)  $Re = 2000$ . The structure of the recirculation region is highlighted using streamlines. The aspect ratio  $\beta$  is equal to 1.

#### 4. Base flows : study of the recirculation region

A typical base flow is depicted in figure 4 for a Reynolds number  $Re = 1500$  and  $\beta = 1$ . The flow is characterized by an upstream radially converging flow turning into an almost parallel jet. However, an important feature is the occurrence of a recirculation region within the thickness of the hole. The vorticity field reaches its maximum near the leading edge, namely the left edge of the hole, and is highly concentrated in the region of maximum shear stress. Figure 5 illustrates the structure of the flow in the close vicinity of the aperture, for  $\beta = 1$ . The recirculation region at  $Re = 800$  takes the form of a narrow bubble trapped close to the upstream corner. As the Reynolds is increased, this bubble expands towards the downstream corner, until it opens up and involves an entrainment of the outer fluid which enters inside the thickness of the plate. Note that for  $Re = 800$ , the recirculation region still contains a bubble of closed streamlines, but detached from the wall. Further on, this bubble disappears and for  $Re = 1600$  the recirculation region is fully open.

The intensity of the recirculation region can be characterized by the maximum level of negative velocity within the thickness of the hole, namely  $U_{max} = \max(-u_{x0})$ . This quantity is plotted in figure 6(a) as function of the Reynolds number for  $\beta = 0.3, 0.6$  and 1. It is observed that in all cases, the recirculation region shows up for  $Re \approx 400$ . The intensity of the recirculation region first grows as the trapped bubble extends to reach the downstream corner, and then decreases as it turns into a fully open one. Not

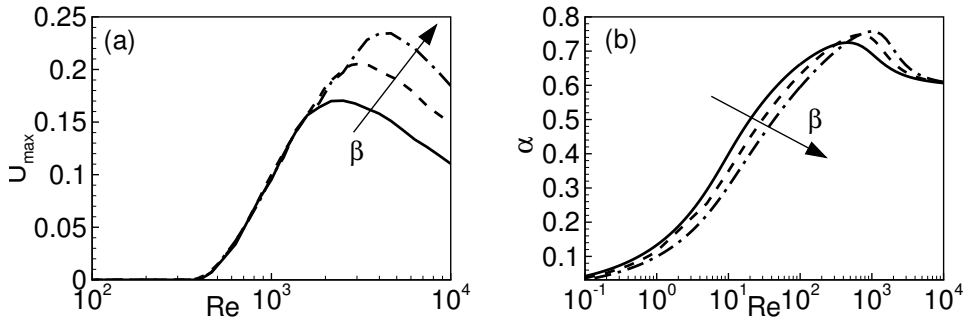


FIGURE 6. (a) Intensity of the recirculation flow inside the hole and (b) vena contracta coefficient as function of  $Re$ . Here we use a solid line for  $\beta = 0.3$ , dashes for  $\beta = 0.6$ , long dashes for  $\beta = 1$ .

surprisingly, the intensity is larger in the case of a thicker hole, as the bubble is able to extend over a longer region.

The steady flow is characterized by the classical phenomenon of the *vena contracta*, i.e. a reduction in the area/diameter of the jet after it emerges from the circular hole. This process produces a pressure loss across the aperture. To estimate this loss, we can apply the Bernoulli theorem along a streamline passing thought the hole:

$$P_{in} - P_{out} = \frac{\rho U_J^2}{2} = \frac{\alpha^2 \rho U_M^2}{2}; \quad (4.1)$$

here, the classical *vena contracta* coefficient  $\alpha$  is introduced as follows:

$$\alpha = (\pi R_J^2) / (\pi R_h^2), \quad (4.2)$$

where  $R_J$  is the jet radius where the flow becomes parallel. There exist several estimations of this coefficient: theoretical prediction by Borda reads  $\alpha = 1/2$  while the hodograph method (Gilbarg 1960) provides  $\alpha \approx 0.61$ .

We document on figure 6(b) the vena contracta coefficient  $\alpha$  deduced from the pressure drop computed from the base flows. It is found that for  $Re \approx 10^4$  the vena contracta coefficient reaches a value close to 0.61 in all cases, again in accordance with litterature results. Note that for the thicker case ( $\beta = 1$ )  $\alpha$  is lower than in the other cases for  $Re \lesssim 100$ , meaning that the pressure drop is weaker, but it is maximal for  $Re \approx 2000$ , a value corresponding approximately to the transition from a closed to an open recirculation region.

Note that Blevins (1984) reports that for  $\beta = 0.3$  the venna contracta coefficient decreases from 0.70 to 0.61 as  $Re$  raises from  $10^3$  to  $10^4$ . This is consistent with our findings. The literature generally attributes this decrease of  $\alpha$  to the laminar-turbulent transition. Since our base-flow solution is strictly laminar, we can rule out this argument. It seems more relevant to attribute the decrease of  $\alpha$  to the transition between attached and fully detached recirculation region.

## 5. Linear results for the forced problem

We turn now to analyse the results obtained by the numerical resolution of the forced problem. We chose two different cases characterized by  $\beta = 0.3$  and  $\beta = 1$ .

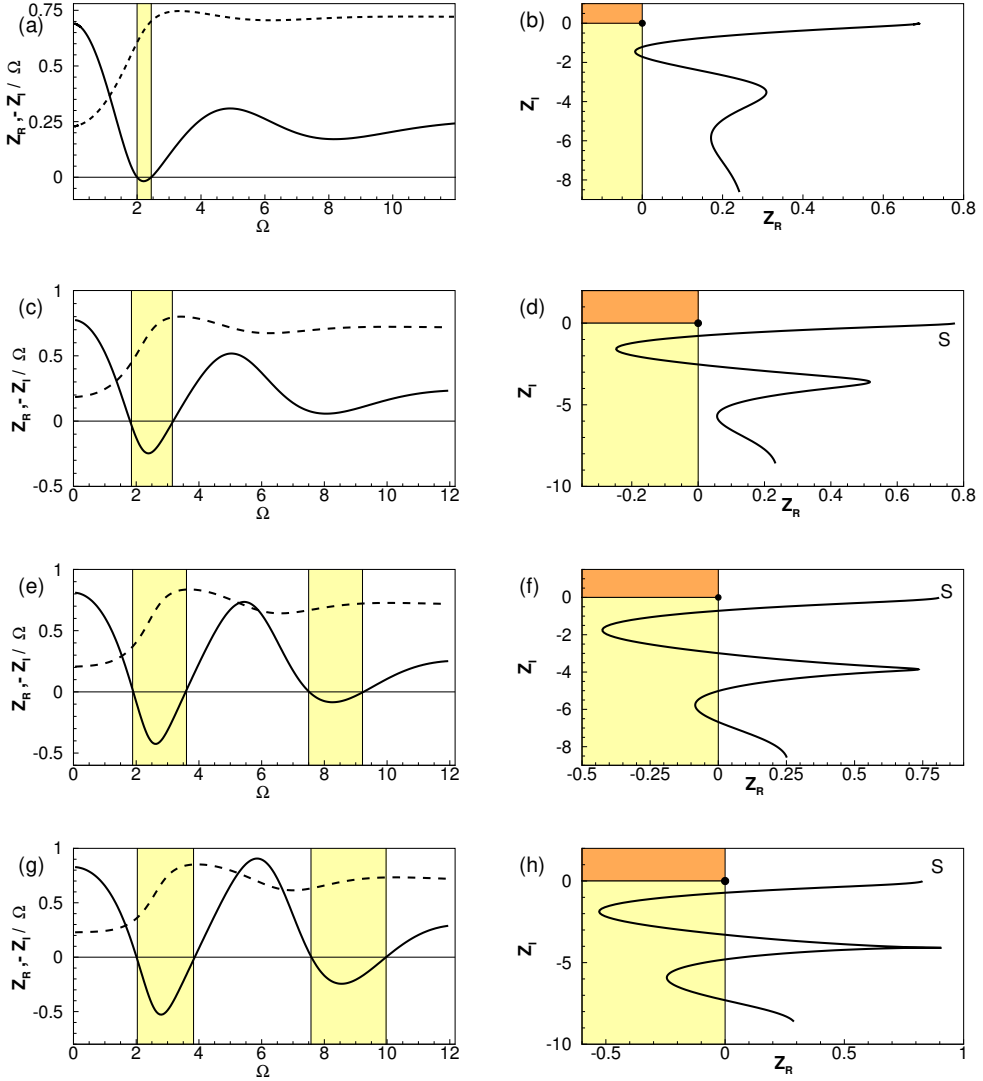


FIGURE 7. Impedance of the flow through a circular aperture with aspect ratio  $\beta = 0.3$ . Left: Plot of  $Z_R$  (solid line) and  $Z_I$  (dashed line) as a function of the perturbation frequency  $\Omega$ ; Right: Nyquist diagrams for (a, b),  $Re = 800$ , (c, d),  $Re = 1200$ , (e, f),  $Re = 1600$ , (g, h),  $Re = 2000$ .

### 5.1. Case $\beta = 0.3$

As previously introduced, the most important quantity associated to the unsteady flow is the impedance  $Z = Z_R + iZ_I$ . This quantity is plotted as function of the frequency in figure 7 for Reynolds ranging from 800 to 2000. The plots in the left column display  $Z_R$  and  $Z_I$  as function of  $\Omega$  (note that as  $Z_I$  is generally negative and increasing with  $\Omega$ , it is convenient to plot  $Z_I/\Omega$ ). The right column display the corresponding Nyquist diagrams.

For  $Re = 800$  (plots (a) and (b)), the system presents a small frequency interval near  $\Omega \approx 2.2$  with negative values of the real part of the impedance  $Z_R$ . As explained in

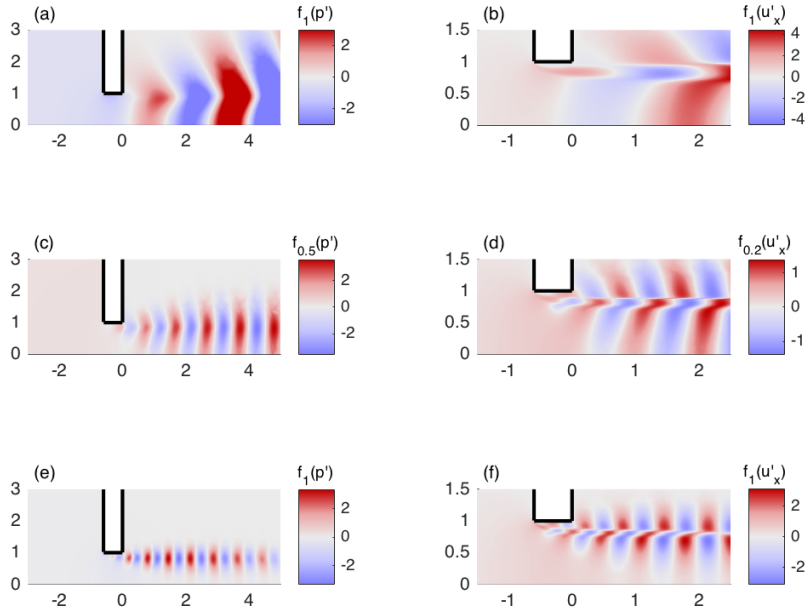


FIGURE 8. Structure of the unsteady flow for  $\beta = 0.3$  and  $Re = 1600$ . Left row: real part of the pressure; right row: real part of the axial velocity. First row (a,b):  $\Omega = 2.6$  and  $Z_h = -0.425 - 1.719i$ , Second row (c,d):  $\Omega = 5.45$  and  $Z_h = 0.736 - 3.861i$ , third row (e,f):  $\Omega = 8.25$  and  $Z_h = -0.085 - 5.762i$ . The color range is rescaled using the distortion function  $f_S$  defined in (5.1).

section 2.3, this property is directly related to a possible instability. On the other hand, the imaginary part  $Z_I$  is always negative in the range of frequencies considered.

As the Reynolds number is increased further, one observes that the region of negative  $Z_R$  gets larger and reaches larger values. Note also that the negative, minimum value of  $Z_R$  is associated to a maximum of  $-Z_I/\Omega$ . Increasing the Reynolds number enlarges the range of  $\omega$  where the system has negative values of  $Z_R$ . The cases (e), (g) associated to  $Re = 1600, 2000$  show a second region of conditional instability for higher frequencies in the range near  $\Omega \approx 8.5$ . This is again associated with a maximum of  $-Z_I/\Omega$ . Note that for Reynolds numbers up to 2000 we do not find a hydrodynamic instability. We recall that the number of unstable modes (absolute instability) is associated to the number of times the contour of the complex impedance  $Z_h$  encircles the origin. This condition is never satisfied in figure 7.

To explain these trends, and in particular the possibility for negative  $Z_R$ , we now depict in figure 8 the structure of the flow perturbation for three values of the frequency, corresponding to the two first minima (8a, b and 8e, f) and a positive maximum (8c, d) of  $Z_R(\Omega)$ . The plots on in the left column display the pressure component  $p'$ , and show that the conditionally unstable cases (8a and 8e) are associated to negative pressure levels in the upstream region, while they are positive in the stable case (8c). Recalling that the

pressure level far away in the downstream region is set to zero, this means that in the unstable cases the fluctuating flow goes against the pressure gradient.

The plots in the right column ( $8b, d, f$ ) display the axial velocity component  $u'_x$ . This quantity displays strong gradients in the region of the shear layer, confirming that the perturbed flow actually corresponds to oscillations of this shear layer, as assumed in the Howe model and represented schematically in figure 1.

An important feature visible on both the pressure plots and the axial velocity plots is that the number of structures of opposite sign (red/blue patches in the figures) within the thickness of the hole is quantified. In effect, we observe respectively 1, 2 and three structures within the hole. This observation for the three first extrema of  $Z_R$  can be generalized as follows : *Minima of  $Z_R$  (potentially unstable situations) are associated to odd number of structures within the thickness while maxima of  $Z_R$  (most stable situations) are associated to even number of structures within the thickness of the hole.* This point was observed for all cases investigated, and will be further demonstrated in next paragraph for  $\beta = 1$ .

Note that, due to the strongly convective nature of the instability, it is impossible to use a linearly scaled color range to visualize the structures both in the region of the hole (where  $p'$  and  $u'_x$  are of order one) and in the jet region (where these quantities may reach levels 100 times larger or higher). This feature was already identified for the zero-thickness case by Fabre *et al.* (2018a). To overcome this difficulty, in figure 8 and subsequent figures, we rescale the color range thanks to a distortion function  $f_S$  defined as

$$f_s(\zeta) = S \text{sign}(\zeta) \log(1 + |\zeta|/S). \quad (5.1)$$

This function is chosen so that the colorange is linear when the plotted quantity  $\zeta$  verifies  $|\zeta| \ll S$  and turns to logarithmic when  $|\zeta| \gg S$ . In the plots the value of  $S$  is adjusted on order to allow the best visualization.

## 5.2. Case $\beta = 1$

We now consider the case of a thicker hole with aspect ratio  $\beta = 1$ . Figure 9 plots the impedance for  $Re$  from 800 to 2000. As in the previous case detailed in sec. 5.1, one can see the existence of several frequency intervals where  $Z_R$  becomes negative.

The real and imaginary part of the impedance  $Z_h$  are always positive for  $Re = 800$  (see fig. 9a ). As a consequence, the associated Nyquist curve plotted in fig. 9b does not cross the  $Z_R = 0$  axis. The system displays two intervals of conditional instability at  $Re = 1200$ , around  $\Omega \approx 2.5$  and  $\Omega \approx 4.7$ , respectively. Note that the real part  $Z_R$  presents larger oscillations than in the corresponding case at  $\beta = 0.3$ .

When the Reynolds number is increased, both real and imaginary parts of the impedance reach very large values. Figure 9e plots  $Z_R$  and  $-Z_I/\Omega$  for  $Re = 1600$  and reveals four intervals of conditional instability and one interval of hydrodynamical instability. Another important result which can be seen in this figure is the existence of true zeros of the impedance. This happens in particular at  $\Omega \approx 2.07$ . This property reveals the existence of a purely hydrodynamical instability as discussed in sec. 3. This point will be further confirmed in sec. 6. Further increasing the Reynolds number to  $Re = 2000$  produces a second interval of hydrodynamical instability around  $\Omega = 4.4$ .

Figure 10 depicts the structure of the oscillating flows for five values of  $\omega$  corresponding to three minima and two maxima of  $Z_R$ . Inspection of these plots allows to confirm the observations made in the previous paragraph for  $\beta = 0.3$ . First, the pressure level is the upstream region is positive (resp. negative) for the conditionally unstable cases where  $Z_R$  is minimum (resp. for the most stable cases where  $Z_R$  is maximum). Secondly, as can be

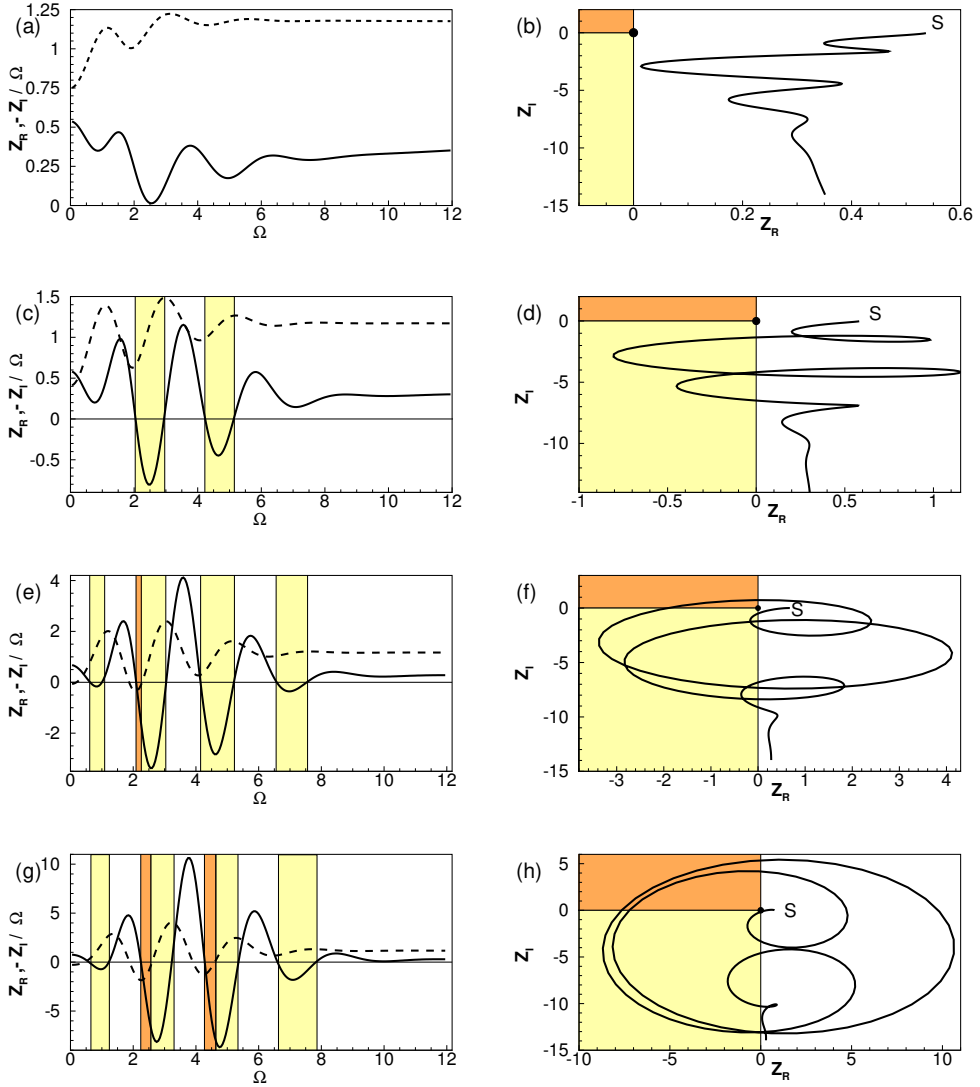


FIGURE 9. Impedance results for  $\beta = 1$ . Left: Plot of  $Z_R$  (solid line) and  $Z_I$  (dashed line) as a function of the perturbation frequency  $\Omega$ ; Right: Nyquist diagrams for (a, b),  $Re = 800$ , (c, d),  $Re = 1200$ , (e, f),  $Re = 1600$ , (g, h),  $Re = 2000$ .

seen especially in the axial velocity plots on the right column, the number of structures (patches of alternating colors) within the thickness of the hole is respectively 1,2,3,4,5 for the cases plotted here. This fully confirms the rule enunciated in the previous paragraph, namely that the conditionally unstable cases correspond to an odd number of structures within the hole.

### 5.3. Parametric study

In the previous sections, we documented the impedance results for  $\beta = 0.3$  and  $\beta = 1$ . In both cases, when increasing the Reynolds number, we observed the emergence of an increasing number of intervals of conditional instability, associated with the crossing

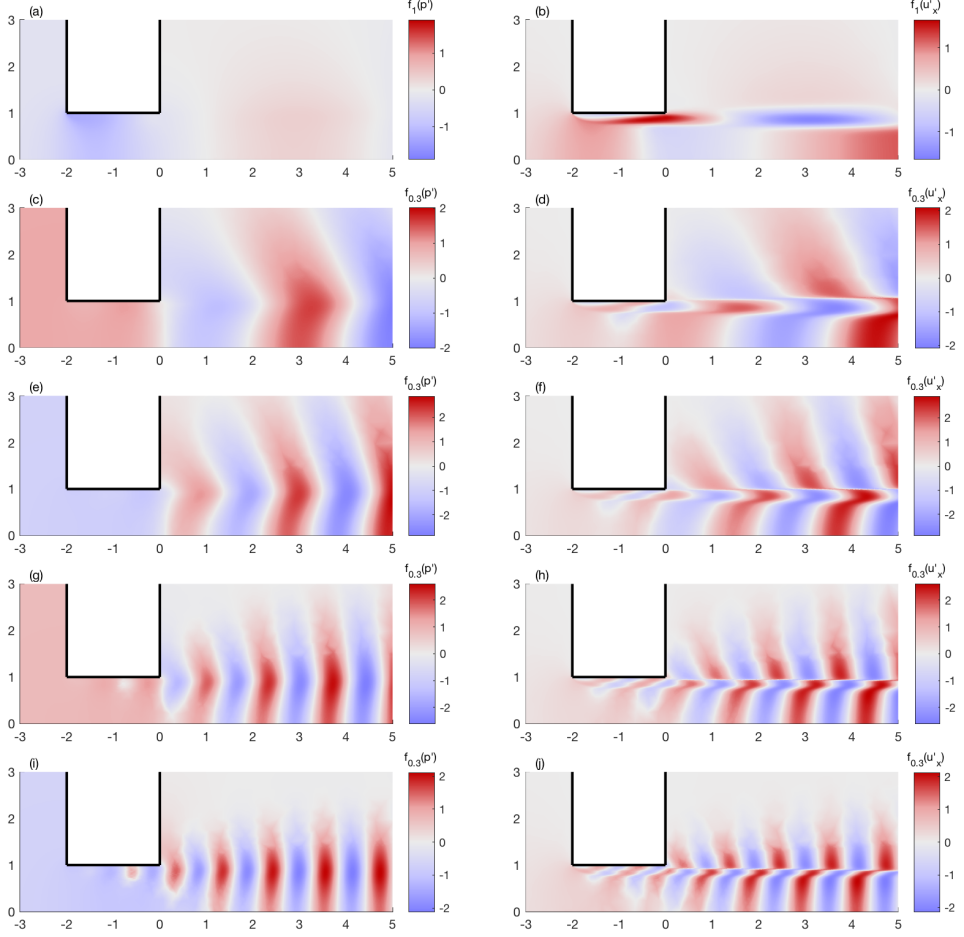


FIGURE 10. Structure of the unsteady flows for  $\beta = 1$  and  $Re = 1600$ . Left: real part of the pressure; right: real part of the axial velocity. First row (a, b)  $\Omega = 0.8$ ; second row (c, d)  $\Omega = 1.6$ ; third row (e, f)  $\omega = 2.5$ ; fourth row (g, h)  $\omega = 3.6$ ; third row (i, j)  $\omega = 4.5$ . The colorrange is rescaled using the distortion function  $f_S$  defined in (5.1).

of the real axis in the Nyquist diagram by successive "loops" of the Nyquist curve. In addition, but only for  $\beta = 1$ , we observed the emergence of an increasing number of purely hydrodynamical instabilities associated to the encircling of the origin by successive loops of the same curve. In this section, we present the results of a parametric study which allowed to identify the regions of conditional and hydrodynamical instabilities in the range  $\beta = [0.1 - 2]$ ;  $Re = [500 - 2000]$ .

Figure 11 shows the critical Reynolds number associated to each instability branch as a function of the aspect ratio  $\beta$ . In this figure, curves labelled C1 to C4 correspond to the first four branches of conditional instabilities, while branches H2 and H3 correspond to the first two branches of hydrodynamical instabilities. We adopted this labelling because these instabilities are associated to the same "loops" in the Nyquist curve as modes C2 and C3. Note that no crossing of the origin was ever observed along the first loop; this is why the figure does not display any H1 branch.

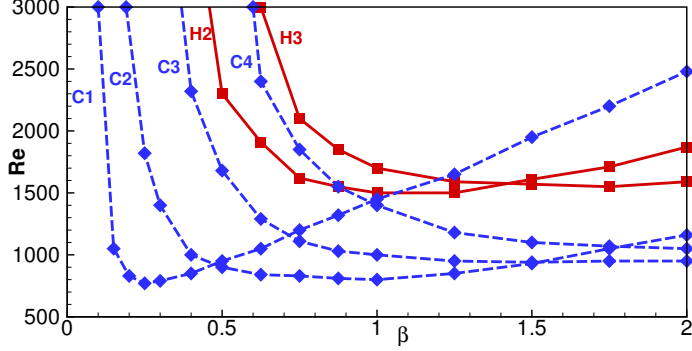


FIGURE 11. Thresholds for the onset of conditional instability ( $C_1$  to  $C_4$ ) and of hydrodynamical instability ( $H_2$  and  $H_3$ ).

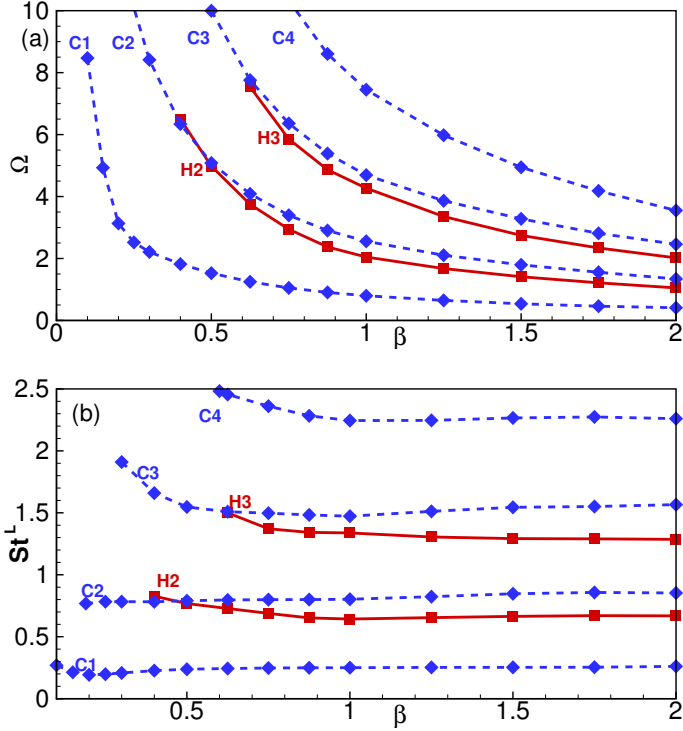


FIGURE 12. Frequencies corresponding to conditional instability ( $C_1$  to  $C_4$ ) and of hydrodynamical instability ( $H_2$  and  $H_3$ ).

For short holes, branch  $C_1$  is the first to become unstable and branches  $C_2$ ,  $C_3$  etc... are only encountered at substantially larger  $Re$ . This is compatible with the results of figure 7 for  $\beta = 0.3$ , which indicates that branch  $C_1$  becomes unstable slightly below  $Re = 800$  and branch  $C_2$  between 1200 and 1600. The situation is different for longer holes as branches  $C_2$ ,  $C_3$  successively become the most unstable ones. For instance, for  $\beta = 1$ , conditional instability first happens along branch  $C_2$  just above  $Re = 800$ , and as  $Re$  is further increased branch  $C_3$ ,  $C_4$  and  $C_1$  are then encountered in this order. This is again fully compatible with the Nyquist diagrams of figure 9.

Hydrodynamical instabilities generally occurs at larger Reynolds than conditional instabilities, and are encountered only for sufficiently thick holes ( $\beta > 0.5$ ). For  $\beta = 1$ , branch H2 becomes unstable for  $Re \approx 1500$  and branch H3 for  $Re \approx 1700$ . This is again fully compatible with the Nyquist representations in figure 9.

We finally notice that for  $\beta < 0.1$  no instability is found in the range investigated. This suggests that the limit case of zero thickness is unconditionally stable, in accordance with the classical model of Howe and our previous investigation of this case (Fabre *et al.* 2018a).

The frequencies associated to the each of the instability branches are plotted in figure 12. We start by plotting the Strouhal number based on the hole radius  $R_h$  as a function of the aspect ratio  $\beta$ . Note that the frequencies associated to hydrodynamical instabilities H2 and H3 closely follows those associated to conditional instabilities C2 and C3, thus confirming our nomenclature choice.

It is interesting to note that all branches indicate that the frequency is inversely proportional to the aspect ratio of the hole. This suggest that instead of the definition  $\Omega$  used up to here, it may be better to define a Strouhal number based on the thickness of the hole as follows:

$$St_L = \frac{fL}{U_M} \equiv \frac{\Omega\beta}{\pi}. \quad (5.2)$$

Plotting results using this definition leads to figure 12b, which confirms that the Strouhal number is almost independant of the aspect ratio for all branches.

The Strouhal number associated to branch C1 corresponds to  $St_L \approx 0.25$ . This value is in good accordance with observations of the leading whistling frequency of jets in a number of experimental and numerical studies. For instance, Kierkegaard *et al.* (2012) indicate  $St \approx 0.26$ , Testud *et al.* (2009), reports values in the range [0.2-0.3], while Anderson (1954) recorded values in the range [0.26-0.29]. This accordance suggests that in all of these works, the instability is of conditional type.

The branch H2 indicates the existence of a purely hydrodynamical instability associated to an almost constant value of the Strouhal number  $St_L \approx 0.65$  in the whole range  $\beta \in [0.4 - 1.5]$ . This implies that a jet through a hole joining two open domains would spontaneously whistle at such frequencies, even in the absence of an acoustic resonator. We are not aware in the recent literature of such an observation, as in all the cited works the hole was fitted at the outlet of a long pipe which played the role of the acoustic resonator needed for conditional instability.

To our knowledge, the only observations of whistling of the flow through a large plate is the work of Bouasse (1929). This author indeed reported that the whistling frequency is proportional to the hole thickness, but unfortunately did not express this result in terms of a Strouhal number.

## 6. Linear stability results

The possible existence of a purely hydrodynamical instability, indicated by the impedance results of the previous sections, will now be confirmed through a global stability approach, which consists of solving an autonomous eigenvalue problem arising from the LNSE, as explained in section 3.

### 6.1. Eigenvalues

The stability characteristics of the base flow are assessed monitoring the evolution of the leading global modes. Figure 13(a) shows the growth rate  $\omega_i$  for three least stable

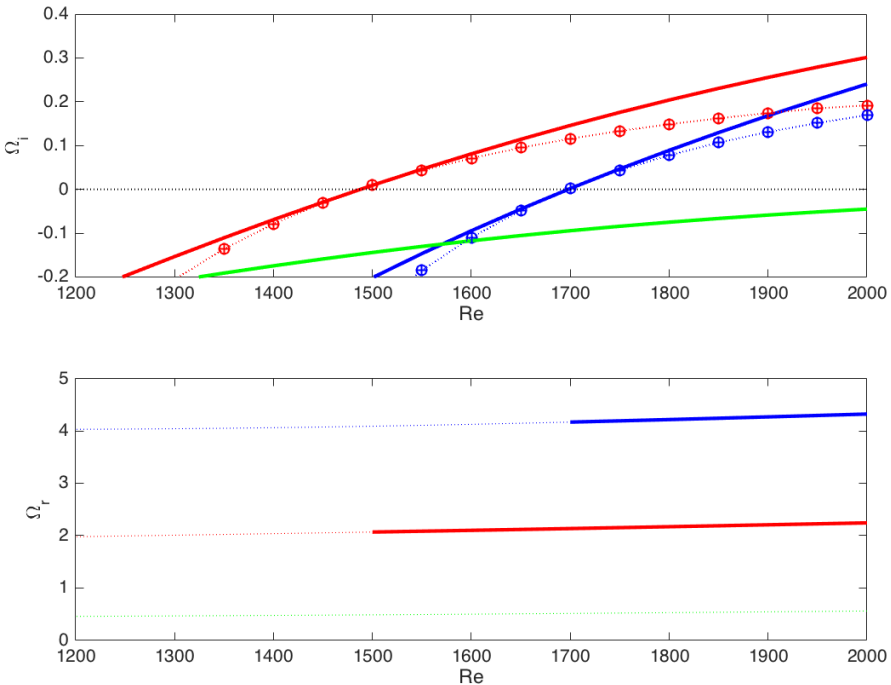


FIGURE 13. Nondimensional growth rates  $\Omega_i = (R_h/U_M)\omega_i$  (a) and oscillation rates  $\Omega_r = (R_h/U_M)\omega_r$  as function of  $Re$ , computed through the linear stability approach (lines) and the order-one expansion based on impedance predictions (symbols).

modes for  $\beta = 1$ . Two of them become unstable in the plotted range of  $Re$ . The first branch becomes unstable at  $Re \approx 1500$  while the second one presents a critical Reynolds number equal to  $Re \approx 1700$ . This is fully compatible with the impedance predictions corresponding to branches H2 and H3 discussed in the previous section.

Figure 13(b) displays the oscillation rate  $\omega_r$  for the same three modes. The three branches display an almost constant value of the radius-based Strouhal number  $\Omega$ . The values for the unstable modes are  $\Omega \approx 2.1$  and  $\Omega \approx 4.2$ , in perfect accordance with the expected values for modes H2 and H3.

Note that figure 13(a–b) displays the existence of a third branch of eigenvalue which is always stable. The corresponding frequency is observed for  $\Omega \approx 0.5$ , which corresponds to a value for which the first "loop" of the Nyquist curve comes close to zero, but does not encircle it. This allows to identify this mode with the "H1" mode which was missing in fig. (11). This mode actually exists as a global mode but remains stable for all values of  $Re$  and  $\beta$  in the investigated range.

As discussed in section 2, in addition to providing an instability criterion, knowledge of the impedance for real  $\omega$  also provides an estimation of the eigenvalues associated to the purely hydrodynamical instability valid in the case where  $\omega_i$  is small. To demonstrate this, we have plotted with symbols in figure 13(a) the prediction of the asymptotic formula (2.7). As can be seen, this formula coincides very well with the numerically computed eigenvalues, but deviations are observed as soon as the dimensionless growth rate exceeds a value of about 0.1.

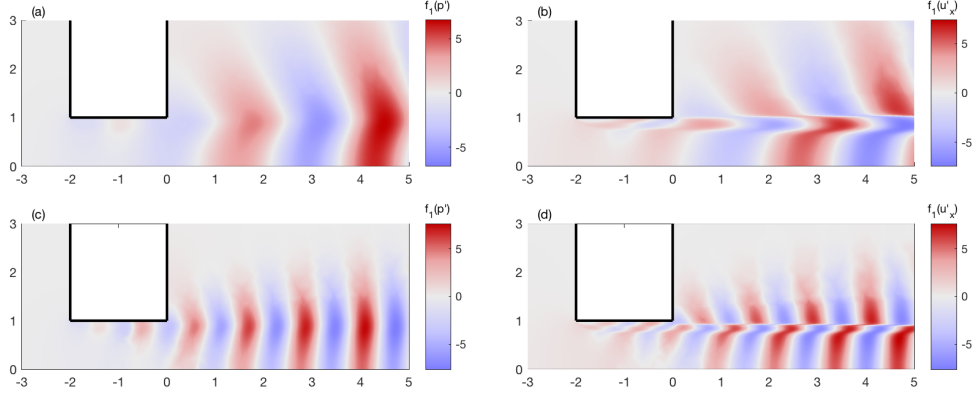


FIGURE 14. Structure of the unstable eigenmodes H2 for  $\beta = 1$ ;  $Re = 1500$  (a, b) and H3 for  $\beta = 1$ ;  $Re = 1570$  (c, d). Same representation as in figure 10.

## 6.2. Eigenmodes and adjoint-based sensitivity

We now depict in the upper part of figure 14 the structure of the unstable modes computed for  $Re = 1500$  and  $Re = 1700$ , respectively. We display the pressure component (a, e) and the axial velocity component (b, f) using the same representation as for the forced structures in figure 10.

The structure of the modes are dominated by axially extended streamwise velocity disturbances located downstream of the aperture and is indeed very similar to the structures obtained in the linearly forced problem. Note that the levels of the pressure components are now tending to zero both upstream and downstream, in accordance with the boundary conditions expected for the purely hydrodynamical instabilities. Apart from this, the eigenmode H2 has strong similarities with the structure of the forced mode C2 for  $Re = 1600$  (figure 10e–f) and the eigenmode H3 with the forced mode C3 (figure 10i–j). The spatial wavelengths are slightly larger than the corresponding forced modes, in accordance with the fact that the frequencies are slightly smaller.

Finally, figure 15 completes the description of the eigenmodes by a plot of their associated adjoint fields and structural sensitivity. The adjoint modes (plots a, b) show that the region of maximum receptivity to momentum forcing is localized near the leading edge of the hole. The spatial oscillations develop in the upstream region. In striking contrast with the direct mode structure, the receptivity decays rapidly both upstream and downstream of the aperture. The distribution of the adjoint fields are also preserved over the range of Reynolds numbers investigated here.

The sensitivity is displayed by plotting the quantity  $S_w$  corresponding to the norm of the structural sensitivity tensor defined by eq. (3.9). The sensitivity for both eigenmodes is essentially localized along the shear layer detaching from the upstream corner of the hole. This confirms that the region responsible for the instability mechanism (the wave-maker region) is the boundary of the recirculation bubble formed within the thickness of the plate.

Interestingly, the structural sensitivity also reaches significant levels in a second region located downstream of the aperture, especially for the mode H3. Note that a similar feature was also observed for instabilities of co-flowing jets (Canton *et al.* 2017). This result indicates that a positive instability feedback enhancing the instability mechanism may also come from the downstream region. This finding may be linked to the role of

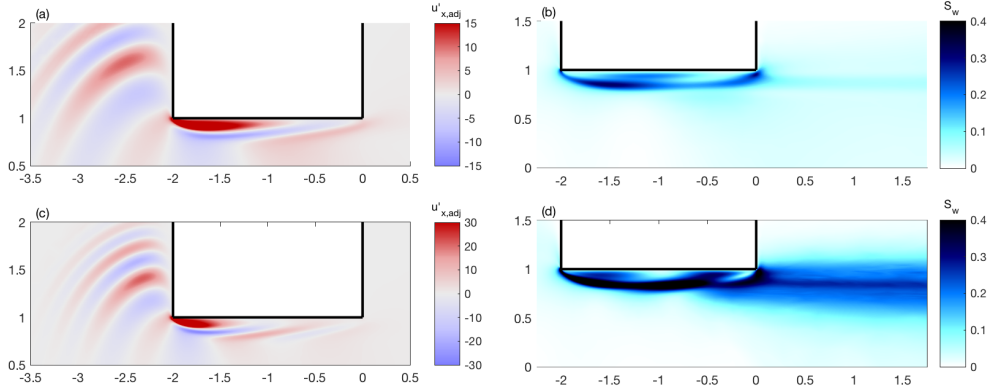


FIGURE 15. Structure of the adjoint eigenmodes (a, c) and structural sensitivity fields (b, d) associated to the eigenmodes plotted in figure 14.

wavepackets propagating along the shear layer bounding the jet on the emergence of self-sustained oscillations.

## 7. Conclusions

In this paper, we studied the laminar viscous jet through a circular aperture in a thick plate. We used a finite element code to solve the numerical problems involved in the stability computations and the impedance computations.

First, we start analysing the base flow features. In particular, we detail the recirculation region inside the hole. The intensity of the flow inside the bubble is found to increase as the thickness of the plate is increased. The vena contracta coefficient present small changes as the aspect ratio  $\beta$  is varied.

Results for the forced problem are presented for two values of  $\beta$ , namely 0.3 and 1.0. We found several regions of conditional instability and no region of hydrodynamical instability in the first case. As a consequence, the Nyquist diagram never encircles the origin for  $\beta = 0.3$ . The second case, on the contrary, is characterized by the occurrence of conditional and hydrodynamical instabilities. We found also a complex zero  $Z_h = 0$  that indicates the existence of a linear perturbation with nonzero flow rate but zero pressure jump across the hole. The main outcome of this study is the parametric investigation discussed in sec. 5.3. Several unstable branches have been identified as the aspect ratio is changed. The Strouhal numbers based on the length of the hole is almost constant over the range considered.

The linear direct global modes present the same structure of the unsteady flow fields. In particular, the spatial distribution is characterized by axially extended oscillations downstream the aperture. The critical Reynolds number for the first and the second branch are found to be respectively  $Re = 1500$  and  $Re = 1700$ . The eigenfrequencies  $\omega$  are almost constant for Reynolds number investigated. The adjoint global modes reveal that the instability is most efficiently triggered in the thin region close to the upstream edge of the hole. The sensitivity maps reach their maximum values in the recirculation region inside the hole. This analysis indicates that the source of instability is linked to the existence of a recirculation region, and this feature is particularly favored by the existence of sharp corners upstream and downstream of the hole. The case of rounded edges is out of the scope of the present paper. However, preliminary results show that rounding the edges result in a more stable configuration.

## Appendix A. Link between impedance and reflection coefficient

The objective of this appendix is to establish the link between the impedance of the aperture and the reflection coefficient of an acoustic wave. For this purpose, we will perform an asymptotic matching between the incompressible "inner" solution investigated in the main part of the paper and a compressible "outer solution" expressed in terms of spherical acoustic waves.

We thus consider an outer solution composed in the upstream domain of an incident convergent spherical wave of amplitude  $A$  and a reflected divergent spherical wave of amplitude  $B$ , and in the downstream region of a transmitted spherical diverging wave of amplitude  $C$ . We use spherical coordinates and assume a pressure field  $p'(r_s, t)$  and a velocity field  $\mathbf{u}' = u'_{rs}(r_s, t)\mathbf{e}_{rs}$  where  $r_s = \sqrt{r^2 + x^2}$  is the spherical radial coordinate and  $\mathbf{e}_{rs}$  is the unit vector in the radial direction. The pressure and axial velocity fields have the classical expressions:

$$p'(r_s, t) = \begin{cases} \frac{A}{r_s} e^{-i(kr_s + \omega t)} + \frac{B}{r_s} e^{i(kr_s - \omega t)} & x < 0; \\ \frac{C}{r_s} e^{i(kr_s - \omega t)} & x > 0. \end{cases} \quad (\text{A } 1)$$

$$u'_{rs}(r_s, t) = \begin{cases} \frac{A}{i\rho\omega} \left( \frac{1}{r_s^2} - \frac{ik}{r_s} \right) e^{-i(kr_s + \omega t)} + \frac{B}{i\rho\omega} \left( \frac{1}{r_s^2} + \frac{ik}{r_s} \right) e^{i(kr_s - \omega t)} & x < 0; \\ \frac{C}{i\rho\omega} \left( \frac{1}{r_s^2} + \frac{ik}{r_s} \right) e^{i(kr_s - \omega t)} & x > 0. \end{cases} \quad (\text{A } 2)$$

where  $k = \omega c_0$  is the acoustical wavenumber and  $c_0$  is the speed of sound. The inner limit ( $r_s \rightarrow 0$ ) of this outer solution can be expressed as follows:

$$p'(r_s, t) \approx \begin{cases} \left( \frac{(A+B)}{r_s} + ik(B-A) \right) e^{-i\omega t} & x < 0; \\ \left( \frac{C}{r_s} + ikC \right) e^{-i\omega t} & x > 0. \end{cases} \quad (\text{A } 3)$$

$$u'_{rs}(r_s, t) \approx \begin{cases} \frac{(A+B)}{\rho i \omega r_s^2} e^{-i\omega t} & x < 0; \\ \frac{C}{\rho i \omega r_s^2} e^{-i\omega t} & x > 0. \end{cases} \quad (\text{A } 4)$$

The outer limit of the inner solution (i.e the incompressible solution considered in the main part of the paper) is a spherical source (resp. sink) of flow rate  $q'$  in the downstream (resp. upstream) domain and reads:

$$u'_{rs}(r_s, t) \approx \begin{cases} \frac{-q'}{2\pi r_s^2} e^{-i\omega t} & x < 0; \\ \frac{q'}{2\pi r_s^2} e^{-i\omega t} & x > 0. \end{cases} \quad (\text{A } 5)$$

$$p'(r_s, t) \approx \begin{cases} \left( p'_{in} + \frac{\rho i \omega q'}{2\pi r_s} \right) e^{-i\omega t} & x < 0; \\ \left( p'_{out} - \frac{\rho i \omega q'}{2\pi r_s} \right) e^{-i\omega t} & x > 0. \end{cases} \quad (\text{A } 6)$$

Note that the latter expressions comprise both the constant levels  $p'_{out}$ ,  $p'_{in}$  and a

subdominant term proportional to  $1/r_s$  which was not mentioned in the main part of the paper. The latter corresponds to the pressure field associated to an unsteady incompressible source/sink.

The matching is done by identifying the coefficients of similar terms in Eqs. (A 3), (A 4), (A 5), (A 6). This leads to:

$$(A + B) = \frac{-\rho i \omega q'}{2\pi}, \quad (\text{A 7})$$

$$ik(B - A) = p'_{in}, \quad (\text{A 8})$$

$$C = \frac{-\rho i \omega q'}{2\pi}, \quad (\text{A 9})$$

$$ikC = p'_{out} \quad (\text{A 10})$$

The two latter relations can be combined with the introduction of the *radiation impedance*  $Z_{rad}$ :

$$Z_{rad} = \frac{p'_{out}}{q'} = \frac{\rho \omega^2}{2\pi c_0} \quad (\text{A 11})$$

The expressions can be eventually combined to express the amplitude reflection coefficient  $B/A$  in terms of the hole impedance  $Z_h$  and the radiation impedance just introduced:

$$\frac{B}{A} = \frac{-Z_h}{Z_h + 2Z_{rad}} \quad (\text{A 12})$$

The energy reflection coefficient  $R$  is eventually deduced as:

$$R = \frac{|B|^2}{|A|^2} = \frac{|Z_h|^2}{|Z_h|^2 + 4Z_{rad}(Re(Z_h) + Z_{rad})} \quad (\text{A 13})$$

These expressions yield the following conclusions :

- the energy reflection  $R$  is larger than 1 (overreflexion condition) if and only if  $Re(Z_h) + Z_{rad} < 0$ . In dimensionless terms, this leads to

$$Z_R + \frac{M\Omega^2}{2\pi} < 0$$

(where  $M$  is the Mach number), which reduces to the simpler condition  $Z_R < 0$  given in section 2 in the limit  $M \ll 1$ .

- $B/A$  is infinite if and only if  $Re(Z_h) + 2Z_{rad} = 0$ . The situation  $B/A = \infty$  corresponds to a situation where a wave is emitted upstream ( $B \neq 0$ ) in the absence of an incident wave ( $A = 0$ ), hence to a spontaneous self-oscillation associated to emission of sound both upstream and downstream. We recognize the definition of the purely hydrodynamical instability described in sec. 2. In dimensionless terms, the condition leads to

$$Z + \frac{M\Omega^2}{\pi} = 0$$

which reduces to the simpler condition  $Z_R = Z_I = 0$  given in section 2 in the limit  $M \ll 1$ .

Note that the assumption of an incident converging spherical wave coming from a semi-infinite space adopted here is questionable; clearly other choices are possible for modelling the upper domain. For instance, the case where the upper domain is a long pipe of radius  $R_p \gg R_h$  and the incident wave is a plane wave can also be considered, and the analysis leads to practically identical conclusions.

	$L_{out}$	$R_{out}$	$L_M$	$L_C$	$L_A$	$\gamma_c$	$R_M$	$R_A$	$x_{max}$	$r_{max}$	$\delta_M$	Adapt.	$N_v$
$M_1$	15	15	0	2.5	17	0.3	5	17	503+149i	337	1	BF+F	19320
$M_2$	20	15	5	1	—	0.5	—	—	20+8i	15	0.5	BF+M	19075
$M_3$	30	20	—	—	—	—	—	—	30	20	1	BF+M+A	30695
$M_4$	60	20	—	—	—	—	—	—	60	20	0.25	BF+F	49999

TABLE 1. Description of meshes  $M_1$ - $M_4$  built for  $\beta = 1$  following four different strategies.  $[L_M, L_C, L_A, \gamma_c, R_M, R_A]$  : parameters defining the coordinate mapping.  $[x_{max}, r_{max}]$ : effective dimensions in physical coordinates.  $\delta_M$ : prescribed value of the maximum grid step. Adapt.: mesh adaptation strategy (see text).  $N_v$  : number of vertices of the mesh obtained at the outcome of the adaptation process.

## Appendix B. Details on the complex mapping technique and mesh validations

As identified in Fabre *et al.* (2018a), a severe numerical difficulty arises in the resolution of the LNSE equations (for both forced and autonomous problems) due to the strong spatial amplification of linear perturbations. In this previous paper, usage of a complex coordinate mapping was proposed as an efficient way to overcome this difficulty. Fabre *et al.* (2018a) demonstrated that in conjunction with mesh adaptation, this method allows both to significantly reduce the required number of mesh points and to extend the range of application of the LNSE up to  $Re \approx 3000$ .

In this appendix we give some detail about the implementation and efficiency of this technique for present study. The technique has been used for both forced (impedance) and autonomous (eigenvalues) computations, but we only document its performances for the autonomous problem, restricting to the case  $\beta = 1$ .

In the present paper, the mappings from numerical coordinates  $(X, Y)$  to physical coordinates  $(x, y)$  are slightly different from the ones used in Fabre *et al.* (2018a), and defined as follows:

$$\begin{aligned} x = \mathcal{G}_x(X) &= L_M + \frac{\frac{X-L_M}{\left[1-\left(\frac{X-L_M}{L_A-L_M}\right)^2\right]^2}}{\left[1+\left(\frac{X-L_M}{2L_C}\right)^2\right]} \quad \text{for } X < L_M, \\ &= X \quad \text{for } L_M < X < L_{out}. \end{aligned} \tag{B1}$$

$$\begin{aligned} r = \mathcal{G}_r(R) &= R_M + \frac{R-R_M}{\left[1-\left(\frac{R-R_M}{R_A-R_M}\right)^2\right]^2} \quad \text{for } X > 0 \text{ and } R_A < R < R_{out}, \\ &= R \quad \text{otherwise} \end{aligned} \tag{B2}$$

Note that the mapping of the  $x$ -mapping involves both an imaginary part (controlled by the parameter  $\gamma_c$ ) and a stretching (controlled by the parameter  $L_A$ .) The difference with Fabre *et al.* (2018a) is the presence of an additional parameter  $L_m$  such that the complex mapping only applies for  $x > L_m$ .

The set of parameters used and the corresponding dimension of the domain in complex coordinates are reported in table 1.

For validation of the method it is essential to demonstrate that the results are effectively

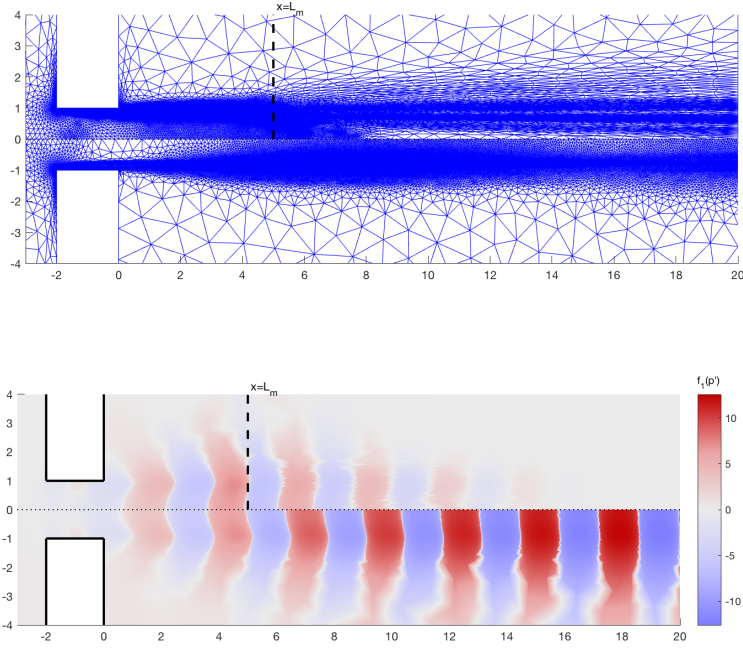


FIGURE 16. (a) Structure of meshes  $\mathbb{M}_2$  (upper) and  $\mathbb{M}_4$  (lower) ; (b) pressure component of the eigenmode H2 as computed using mesh  $\mathbb{M}_2$  (upper) and  $\mathbb{M}_4$  (lower).

independent of the values of the parameters. In the present study we have mainly used two kind of meshes involving complex mapping, with properties detailed in table 1. The first one, named  $\mathbb{M}_1$ , and already plotted in fig. 3, is very similar to the one used in Fabre *et al.* (2018a) for the case of the zero-thickness hole. This kind of mesh has been used for the impedance-based parametric study of section 5.3. On the other hand, since the coordinate mappings applies for  $x > L_M = 0$ , it is not suited to represent the linear forced flow and eigenmode structures. The second one kind of mesh, named  $\mathbb{M}_2$ , has no stretching (thus parameters  $L_A$  and  $R_A$  are not relevant) but only complex mapping. This kind of mesh has been used to plot the structures (figures 8,10 and 14) since complex mapping only applies for  $x > L_M = 5$ , outside of the chosen range of these figures. The two meshes also differ by the mesh adaptation strategy : mesh  $\mathbb{M}_1$  is adapted to the base flow for  $RE = 2000$  and two forced flow structures computed for two values of  $\Omega$  spanning the range of the parametric study, namely  $\Omega = 0.5$  and  $\Omega = 4.5$ , following the same strategy as in Fabre *et al.* (2018a). On the other hand, mesh  $\mathbb{M}_1$  is adapted to the base flow and the two leading eigenmodes H1 and H2, following the same strategy as in Fabre *et al.* (2018b).

For validation purposes, we have also designed two meshes  $\mathbb{M}_3$  and  $\mathbb{M}_4$  which do not involve coordinate mapping. These meshes are designed with a longer axial dimension  $L_{out}$ , and are characterized and are significantly heavier in terms of number of vertices.

Figure 16(a) displays the structure of meshes  $\mathbb{M}_2$   $\mathbb{M}_4$ . It is found that the mesh adaptation strategy used for mesh  $\mathbb{M}_2$  is most efficient to concentrate the grid points

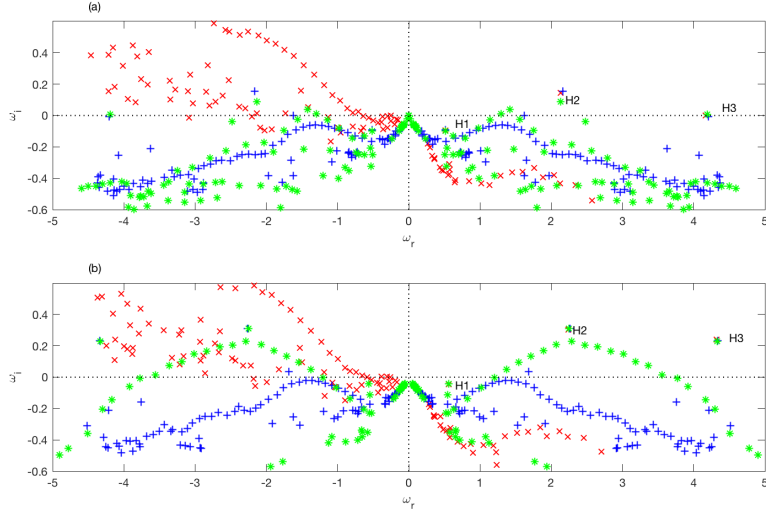


FIGURE 17. Spectra computed with three different meshes :  $\times$  (red online): mesh  $M_1$  (complex mapping);  $*$  (green online): mesh  $M_3$  (no mapping,  $X_{max} = 30$ );  $+$  (blue online): mesh  $M_4$  (no mapping,  $X_{max} = 60$ ). (a):  $\beta = 1$ ;  $Re = 1700$  ; (b):  $\beta = 1$ ;  $Re = 2000$

in the most significant regions of the flow (inside the hole) while  $M_4$  concentrates a much larger number of points in the far downstream regions.

Figure 17 superposes the numerically computed spectra using meshes  $M_1$ ,  $M_3$  and  $M_4$  for  $Re = 1700$  and  $2000$ . As usual, along with the eigenvalues of the physically relevant modes  $H_1$ ,  $H_2$ ,  $H_3$ , the spectra display a large number of spurious eigenvalues. As can be seen, both meshes  $M_3$  and  $M_4$  lead to the presence of spurious modes in the unstable part ( $\omega_i > 0$ ) of the complex plane, and as the Reynolds number is increase they come dangerously close to the physical eigenvalues. On the other hand, the complex mapping used for mesh  $M_1$  results in a good separation between the physical eigenvalues and the spurious ones, which are substantially shifted in the stable part ( $\omega_i < 0$ ) of the complex plane. Note, however, that use of the complex mapping does not allow to compute the complex conjugates of modes  $H_1$ ,  $H_2$ ,  $H_3$  located in the  $\omega_r < 0$  half-plane. For reasons discussed in Fabre *et al.* (2018a), using a complex mapping with  $\gamma_c > 0$  only allows to suppress the spatial amplification of linear forced structures (or eigenmodes) with  $\omega_r > 0$ . Instead, choosing  $\gamma_c < 0$  would give access to the other half of the spectrum.

Table 2 displays the eigenvalues  $H_1$ ,  $H_2$ ,  $H_3$  computed for  $Re = 1600$  and  $2000$  using all meshes considered here. The table confirms that the results obtained using complex mapping are independent upon the values of the parameters (value for  $M_1$  and  $M_2$  are very close to each other despite the fact that the parameters are very different). They also show that the meshes  $M_3$  and  $M_4$  are less reliable despite the fact that they contain a larger number of vertices.

Finally, figure 16(b) depicts the structure of the eigenmode  $H_2$  computed using meshes  $M_2$  and  $M_4$  for  $Re = 1600$ . As the complex mapping for mesh  $M_2$  only applies for  $x > L_m = 5$ , the structure for  $x < L_m$  is expected to be identical as when computed without this method. The figure confirms that this is effectively the case. On the other hand, for  $x > L_m$  the eigenmode computed in physical coordinates still displays a spatial amplification up to a very large downstream distance. On the other hand, the complex mapping results in a suppression of this spatial amplification.

	$Re = 1600$		
	H1	H2	H3
$M_1$	-0.1176i + 0.5000	0.0809i + 2.1007	-0.0942i + 4.1245
$M_2$	-0.1164i + 0.5014	0.0813i + 2.1108	-0.0925i + 4.1207
$M_3$	-0.1259i + 0.5017	0.13916i + 2.1051	-0.1051i + 4.1359
$M_4$	-0.1189i + 0.5017	0.0840i + 2.0953	-0.1955i + 4.0984

	$Re = 2000$		
	H1	H2	H3
$M_1$	-0.0450i + 0.5610	0.3010i + 2.2434	0.2408i + 4.3205
$M_2$	-0.0438i + 0.5619	0.3042i + 2.2476	0.2427i + 4.3170
$M_3$	-0.0421i + 0.5645	0.3114i + 2.2467	0.2287i + 4.3268
$M_4$	-0.0420i + 0.5628	0.2965i + 2.2399	0.1232 + 4.2807

TABLE 2. Eigenvalues computed with four different meshes for  $RE = 1600$  and  $Re = 2000$   
( $\beta = 1$ )

Note that figure 16(b) makes use of a nonuniform colormap by plotting  $f_S(p')$  as explained in sec. 5.1. Without this trick it would be impossible to give a good representation of the structure, as the maximum values  $p'$  are of order  $1.8 \cdot 10^3$  and  $3 \cdot 10^5$  for  $M_2$  and  $M_4$ , respectively. Hence use of the complex mapping limits the round-off errors due to the very large maximal levels reached far downstream. Note that on the other hand, this visualization method enhances the numerical imprecision in the external parts of the flow ( $|R| > 2$ ) where the mesh is less refined (but where mesh refinement is not necessary for accurate computation of the eigenvalues).

## REFERENCES

- ANDERSON, A. B. C. 1954 Orifices of small thickness-diameter ratio. *The Journal of the Acoustical Society of America* **26**, 21–25.
- BELLUCCI, V., FLOHR, P., PASCHERAIT, C. O. & MAGNI, F. 2004 On the use of helmholtz resonators for damping acoustic pulsations in industrial gas turbines. *Journal of engineering for gas turbines and power* **126** (2), 271–275.
- BLEVINS, R. D. 1984 *Applied Fluid Hydrodynamics Handbook*. New-York: Van Nostrand Reinhold.
- BOUASSE, HENRI 1929 *Instruments à vent*. Impr. Delagrave.
- CANTON, J., AUTERI, F. & M., CARINI 2017 Linear global stability of two incompressible coaxial jets. *J. Fluid Mech.* **824**, 886–911.
- CITRO, V., GIANNETTI, F., P., LUCHINI & AUTERI, F. 2015 Global stability and sensitivity analysis of boundary-layer flows past a hemispherical roughness element. *Physics of Fluids* **27**, 84110.
- CITRO, V., TCHOUFAG, J., FABRE, D., GIANNETTI, F. & P., LUCHINI 2016 Linear stability and weakly nonlinear analysis of the flow past rotating spheres. *Journal of Fluid Mechanics* **807**, 62–86.
- CONCIAURO, G & PUGLISI, M 1981 Meaning of the negative impedance. *NASA STI/Recon Technical Report N* **82**.
- ELDREDGE, J. D., BODONY, D. J. & SHOEYBI, M. 2007 Numerical investigation of the acoustic behavior of a multi-perforated liner. *Am. Inst. Aeron. Astron.* (2007-3683).
- FABRE, D., LONGOBARDI, R., BONNEFIS, P. & LUCHINI, P. 2018a The acoustic impedance of a laminar viscous jet through a thin circular aperture. *Journal of Fluid Mechanics, Under review*.
- FABRE, D., SABINO, D. FERREIRA, CITRO, V., BONNEFIS, P. & GIANNETTI, F. 2018b A

- practical review to linear and nonlinear approaches to flow instabilities. *Appl. Mech. Rev.* (*submitted*) .
- GILBARG, D 1960 *Encyclopedia of Physics; Volume IX, Fluid Dynamics III. Jets and Cavities*. Springer-Verlag.
- HOWE, M. S. 1979 On the theory of unsteady high reynolds number flow through a circular aperture. In *Proceedings of the Royal Society of London A: Mathematical, Physical and Engineering Sciences*, , vol. 366, pp. 205–223. The Royal Society.
- HUERRE, P. & MONKEWITZ, P. A. 1990 Local and global instabilities in spatially developing flows. *Annu. Rev. Fluid Mech.* **22**, 473–537.
- JING, X. & SUN, X. 2000 Effect of plate thickness on impedance of perforated plates with bias flow. *AIAA journal* **38** (9), 1573–1578.
- KIERKEGAARD, AXEL, ALLAM, SABRY, EFRAIMSSON, GUNILLA & ÅBOM, MATS 2012 Simulations of whistling and the whistling potentiality of an in-duct orifice with linear aeroacoustics. *Journal of Sound and Vibration* **331** (5), 1084–1096.
- LUCHINI, P. & BOTTARO, A. 2014 Adjoint equations in stability analysis. *Annu. Rev. Fluid Mech.* **46**, 493–517.
- RAYLEIGH, J. W. S. 1945 *The theory of sound*.
- SU, J., RUPP, J., GARMORY, A. & CARROTTE, J. F. 2015 Measurements and computational fluid dynamics predictions of the acoustic impedance of orifices. *Journal of Sound and Vibration* **352**, 174–191.
- TESTUD, P., AUREGAN, Y., MOUSOU, P. & HIRSCHBERG, A. 2009 The whistling potentiality of an orifice in a confined flow using an energetic criterion. *Journal of Sound and Vibration* **325**, 769–780.
- YANG, D. & MORGANS, A. S. 2016 A semi-analytical model for the acoustic impedance of finite length circular holes with mean flow. *Journal of Sound and Vibration* **384**, 294–311.